The Band Structure of Polycrystalline Al_2O_3 and its Influence on Transport Phenomena

A.H. Heuer[*,] M. Zahiri Azar[*], H. Guhl[**,***], W.M.C. Foulkes[***], B.Gleeson [****], T. Nakagawa[*,*****], Y. Ikuhara[******] and M.W. Finnis[**,***]**

Abstract

The electronic (band) structure of polycrystalline Al_2O_3, in particular the density of near-band edge grain boundary localized states, plays a significant role in a host of high temperature phenomena, including sintering, high temperature creep, oxygen permeability in dense "dry" Al_2O_3 ceramics, and Al_2O_3 scale formation on Al_2O_3 scale-forming alloys. All these phenomena involve creation or annihilation of charged point defects (vacancies and/or interstitials) at grain boundaries and interfaces, and must of necessity involve electrons and holes. Thus, the density of states (DOS) associated with grain boundaries in Al_2O_3 assume great importance, and has been calculated using DFT for both nominally un-doped and Y-doped Σ7 bi-crystal boundaries. These quantum mechanical calculations must be taken into account when considering why Y_2O_3 segregation to Al_2O_3 grain boundaries is so effective in enhancing high temperature creep resistance of polycrystalline Al_2O_3, and in understanding the reactive element effect in Al_2O_3 scale-forming alloys. Finally, a case will be made that grain-boundary diffusion is mediated by the migration of a class of grain boundary ledge defects called ***disconnections****, which are characterized by a step height* h *and a Burgers vector* **b***.*

*** Dept. of Materials Science and Engineering, Case Western Reserve University, Cleveland OH 44106-7204 USA**
**** Dept. of Materials, Imperial College, London, SW7 2AZ UK**
***** Dept. of Physics, Imperial College, London, SW7 2AZ UK**
****** Dept. of Mechanical Engineering and Materials Science, Univ. of Pittsburgh, Pittsburgh, PA 15261 USA**
******* Elements Strategy Initiative for Structural Materials, Kyoto University, 606-8501 Japan**
******** Inst. of Engineering Innovation, Univ. of Tokyo, 113-8656 Japan**

I. Introduction

Segregation of Y_2O_3, ZrO_2, HfO_2 and rare earth oxides such as La_2O_3, Lu_2O_3, and Nd_2O_3 to grain boundaries in polycrystalline Al_2O_3 causes profound changes in its properties and performance, most notably in improving high temperature creep resistance (1, 2), and enhancing the oxidation resistance of Al_2O_3 –scale forming alloys containing Y, Zr, and Hf (the so-called "Reactive Element" (RE) effect) (3). Given that both the creep resistance and the oxidation resistance are usually thought to be diffusion-controlled, and given the sluggish lattice diffusion kinetics of both oxygen and Al in Al_2O_3 (4), explanations for these enhanced performances almost always involve purported changes in grain boundary diffusivities arising from dopant segregation.

Unfortunately, there appear to be no direct measurements of dopant effects on Al grain boundary diffusivity, δD_b^{Al} (δ is the nominal width of the region providing the enhanced diffusivity). However, the effect of segregated Y_2O_3 on oxygen grain boundary diffusion in Al_2O_3, δD_b^{oxy}, has been studied in polycrystalline Al_2O_3 (5) and in a $\Sigma 31$ {7 -11 4 0} bi-crystal boundary (6). Y_2O_3 decreased δD_b^{oxy} by about 50*x* in the polycrystals and about 10*x* in the bi-crystals. An ostensibly related improvement in high temperature creep resistance by up to $\sim 10^3$ was reported in doped polycrystalline Al_2O_3 (1, 2). Y_2O_3-doped Al_2O_3 proved to be more creep resistant than La^{3+}-, Nd^{3+}-, or Zr^{4+}-doped materials, although all dopants improved creep resistance compared to nominally un-doped Al_2O_3.

In the case of Al_2O_3 scale growth, segregation of Y_2O_3 and other RE oxides to scale grain boundaries decreased the apparent Al grain boundary diffusivity by ~4x, but had little or no effect on the apparent oxygen grain boundary diffusivity (3). In comparing the effect of single dopant additions to a Ni-20Al-5Cr base alloy on isothermal oxidation resistance at 1150˚C (7), 0.1% or 0.05% additions of Hf to the base alloy were more efficacious than similar Y additions, and 0.05% Y addition to this alloy was more efficacious than 0.1% Y addition.

The most common explanation for these dopant effects is that these ions on Al^{3+} grain boundary sites block critical diffusion paths because of steric (ionic size) effects. However, there are problems with this point of view. With regard to the RE effect, for example, Hf^{4+} is more effective than Y^{3+}; yet the ionic radius of Hf^{4+} is intermediate to those of Al^{3+} and Y^{3+}, *i.e.*, the ionic radius of Al^{3+} is 67.5 pm, that of Y^{3+} 104.0 pm, and that of Hf^{4+} 86.0 pm (8). Further, there appears to be poor correlation between ionic radius and enhanced creep resistance when La^{3+}, Lu^{3+}, Nd^{3+}, or Zr^{4+} are substituted for Y^{3+}(1, 2). It has also been suggested (9) that changes in bond strength or oxygen coordination of these segregated cations may play a role in these phenomena.

In two earlier papers (10, 11), we put forward the novel suggestion that electronic effects, particularly the effect of Y segregation on the density of near-band edge grain boundary localized states, necessary for the generation of electronic defects (electrons and holes), might be important in understanding the favorable effect of these grain

boundary segregants on the oxidation resistance of RE-containing alloys such as FeCrAlYs and NiCrAlYs. Here, we consider the possibility that these band structure considerations are also important in understanding the favorable effect of such segregants on the creep resistance of doped Al_2O_3.

These notions provided motivation for DFT (density functional theory) calculations of the atomic and electronic (band) structures of two Σ7 bi-crystal boundaries with different boundary planes (12), which exhibited a factor of about 1,000 difference in δD_b^{oxy} (13). The lower diffusivity boundary has a more ordered and compact structure and fewer near-band edge defect states than the less compact, higher diffusivity boundary, and we inferred that high concentrations of such near-band edge defect states are a general feature of random high angle grain boundaries in Al_2O_3. Finally, the band structure of a Σ7 bi-crystal boundary containing segregated Y_2O_3 reveals a significant effect of Y_2O_3 on the concentration of these near-band edge defect states.

These band structure considerations constitute the *raison d'être* for this paper. We first review recent studies on oxygen permeability in dense Al_2O_3 ceramics, as these show particularly clearly the importance of electronic defects in vacancy production/annihilation at grain boundaries and interfaces. This is followed by a discussion of the DFT calculations of the Σ*7* boundaries, and considerations of the improved creep resistance of Y_2O_3-doped Al_2O_3 and improved oxidation resistance of RE-containing alloys. We conclude by reviewing enhanced grain boundary diffusion in Al_2O_3.

II. Oxygen Permeability in Polycrystalline Al_2O_3

Dense polycrystalline Al_2O_3, and Al_2O_3 doped with 0.1 mol% Y_2O_3, Lu_2O_3 or HfO_2, were subject to $p(O_2)$ gradients at elevated temperatures and the steady state oxygen permeation rates measured (14-20). Oxygen permeation occurs solely by grain boundary diffusion in these experiments, as identical experiments with single crystal sapphire showed no permeation, consistent with the very sluggish lattice diffusion kinetics in Al_2O_3 (4). Grain boundary diffusivities derived from these permeability measurements will be compared to tracer data in Section VI.

Here, we are concerned with the effects of Y-, Lu-, and Hf-doping on oxygen permeability (17-19), and note that, as expected, extensive segregation of these solutes to Al_2O_3 grain boundaries was observed. Particles of $Y_3Al_5O_{12}$ (yttrium aluminum garnet or YAG), $Lu_3Al_5O_{12}$ (LAG), and monoclinic HfO_2 (*m*-HfO_2) were also present (18), indicating that the solubility limit for Y_2O_3, Lu_2O_3 and HfO_2 in Al_2O_3 is below 0.1 mol%.

Y and Lu doping suppressed oxygen grain boundary mobility by ~ 1/3 but had essentially no effect on Al grain boundary mobility, whereas Hf doping had essentially no effect on oxygen mobility but decreased Al grain boundary mobility by ~1/2

(17-19). These effects, which are generally at variance with Al_2O_3-scale growth behavior on RE-doped alloys [3], were attributed to grain boundary "strengthening" and/or steric "site blocking". In Sections III - V, we will argue that band structure issues must also be considered.

The general picture of oxygen permeability in these experiments may be summarized as follows. For convenience, we refer to *low pressure* experiments as those in which the high and low oxygen pressures that established the $p(O_2)$ gradient were 1Pa and 10^{-3}Pa (or smaller), respectively, and *high pressure* experiments as those in which the high and low oxygen pressures were 10^5 Pa (or slightly smaller), and 1Pa, respectively. Oxygen permeation involving oxygen grain-boundary diffusion predominates in the low-pressure experiments, but a more complex process involving Al grain boundary diffusion occurs at high oxygen pressures. Firstly, in the low-pressure experiments, dissociative adsorption of O_2 molecules occurs such that oxygen molecules at the 1 Pa interface dissolve in the lattice, becoming lattice oxygen ions, and consuming oxygen vacancies in the process. New lattice sites are not created. The concentration gradient of oxygen vacancies thus established drives them towards the 1Pa interface, with a counter flow of oxygen ions to the opposite low-pressure interface, where they form O_2 molecules, which then enter the local ambient. These reactions clearly allow an effective permeation of oxygen molecules through the dense ceramic.

Oxygen permeation during the high-pressure experiments is apparently quite different. O_2 molecules still dissociate to form lattice oxygen ions at the high-pressure interface, but the lack of oxygen vacancies for them to enter the lattice means that they do not dissolve in the existing lattice but define new lattice sites, automatically creating associated Al vacancies, either as new lattice sites available to Al ions, or by directly pulling out the Al ions and injecting the Al vacancies, in the ratio required to balance stoichiometry. At the same time, lattice oxygen ions at the 1 Pa interface pair up in the presence of arriving Al vacancies to form O_2 molecules, which desorb and enter the local ambient. This has the effect of causing molecular units of Al_2O_3 to disappear from the 1 Pa interface. The Al vacancies created at the high-pressure interface flow down the vacancy concentration gradient to the low-pressure interface, causing a counter-flow of Al ions. These Al ions, meeting the oxygen ions from the oxygen dissociation reaction, create "new" Al_2O_3; in effect, the oxygen permeation caused a displacement of oxide from the low $p(O_2)$ to the high (pO_2) interface via grain-boundary diffusion.

The above description of the process neatly explains why ridges are formed in the high-pressure experiments, where the grain boundaries emerge at the high-pressure surfaces, and not on the other surfaces; it is because it is only on these surfaces that new oxide lattice sites are being created by the diffusion process. We should nevertheless ask whether there are alternative plausible mechanisms at the atomic scale that would account for the experimental data, other than conventional vacancies on cation and anion sites. Consider first simple flow of interstitials as a transport mechanism. In the high $p(O_2)$ experiments the concentration of Al interstitials would be suppressed, so they would be most unlikely to be the means for transferring Al from the lattice to the fresh material of the ridges. Conversely, oxygen interstitials would be

unlikely in the low $p(O_2)$ scenario, and if they were responsible for the oxygen transport, no ridges of new oxide would appear. An unconventional mechanism, which is consistent with the above evidence and some other information to be discussed below, is that the vacancies are actually incorporated into the jogs of disconnections, which are a special type of interface line defect on the grain boundaries (21).

This interpretation of the oxygen permeability experiments in terms of flows of charged vacancies implies a flow of electrons and holes in order to balance the charges; thus, at the low pressure interface in the low-pressure experiments, molecular oxygen formation occurs via Eqn. [1]

$$O_O^x \rightarrow V_O^{\cdot\cdot} + \tfrac{1}{2}O_2 + 2e' \qquad [1]$$

with the reverse reaction occurring at the higher pressure interface.

At the high pressure interface in the high-pressure experiments, O_2 molecules are absorbed via Eqn. [2].

$$\tfrac{3}{2}O_2 \rightarrow 2V_{Al}''' + 3O_O^x + 6h^{\cdot} \qquad [2]$$

with the reverse reaction occurring at the low pressure interface.

These equations emphasize that the electronic structure of Al_2O_3 is crucial to oxygen grain-boundary permeation, and to vacancy production/annihilation in general.

Equations [1] and [2] imply *p*-type ionic charge transport at low pressures but *n*-type at high oxygen pressures. The accompanying electronic transport, necessary to maintain charge neutrality in these oxygen permeability experiments (and in Al_2O_3 scale growth) is, by the same token, *n*-type and *p*-type, respectively (10).

Using the law of mass action together with the assumption of electrical neutrality, it is easy to show that the permeation rate should vary as $p(O_2)^{-1/6}$ at low $p(O_2)$ and as $p(O_2)^{+3/16}$ at high $p(O_2)$, as is observed (Fig. 1). As already mentioned, the permeation rates are controlled by δD_b^{oxy} at low oxygen pressures but by δD_b^{Al} at high oxygen pressures.

Figure 1 is a Brouwer diagram for Al_2O_3 resulting from the oxygen-permeation experiments. Given that Al_2O_3 is not usually considered a non-stoichiometric oxide, the pressure at which the *n*-*p* transition occurs for Al_2O_3, ~0.1Pa, denotes a different phenomenon from that pertaining to transition metal oxides such as NiO and CoO, which are non-stoichiometric and therefore exhibit a clear dependence of electrical conductivity on external $p(O_2)$.

For Al_2O_3, the *n*-*p* transition must involve a $p(O_2)$ dependence of the Fermi level (the chemical potential of the electrons) and depends on the density of near-band edge

grain boundary defect states. In fact, a recent DFT calculation of *Σ13* and *Σ31* bi-crystal boundaries (22) found the expected $p(O_2)$ dependence of the Fermi level as well as a $p(O_2)$ dependence of the formation energies of oxygen and Al vacancies, and a significant narrowing of the band gap to about 60% of the single crystal value, through lowering of the conduction band minimum. One caveat is that the defect energies at the boundary were not calculated, just the effect of the boundary on the bulk concentrations. Thus, the ratio of defect concentrations at the boundary might be different. Finally, just as in the case of Al_2O_3 scale formation (11), electric fields will develop during the permeation experiments, although these have not been explicitly discussed in the original publications (14-20) and will be discussed further in Section VI.

The permeation rates have been used to determine grain-boundary diffusivities, δD_{gb}, for oxygen at low $p(O_2)$s and for Al at high $p(O_2)$s, as is shown in Fig. 2. As it is unlikely that the mobility of the mobile species depends on $p(O_2)$, the $p(O_2)$ dependence shown in Fig. 2 most likely arises from a $p(O_2)$ dependence of the concentrations of mobile species arising from Eqns. [1] and [2].

III. The Atomic and Electronic Structures of *Σ7* Grain Boundaries

Equations [1] and [2] in the previous section make clear the importance of electrons and holes for vacancy production and annihilation in Al_2O_3. The availability of these electronic defects must arise from near-band edge states.

We now review recent DFT calculations (12) of the atomic structure and DOS (density of states) of nominally un-doped Σ*7{2-310} (Σ7m)* and Σ*7{4-510} (Σ7a)* bi-crystal boundaries, and provide DFT results for a Σ*7{2-310}* boundary containing a Y_2O_3 segregant. (As noted already, and as is shown in Fig. 11 below, the *Σ7a* boundary exhibited much faster oxygen grain boundary diffusivities than did the Σ*7m* boundary (13).) Using the atomic coordinates of the calculated lowest energy structures of the two *Σ7* bi-crystal boundaries as input for HREM image simulations, reasonable agreement with the experimental HREM images was obtained (12).

The *Σ7m* and *Σ7a* calculations employed a "Simulated Annealing" molecular dynamics (MD) approach to find the lowest energy structure for a given Al_2O_3 boundary (12). A high temperature structure for each *Σ7* boundary, with a large excess energy, starting in a disordered liquid state, was set up in the computer with periodic boundary conditions, then slowly cooled and alternately compressed and expanded to find the structure with the minimum energy, thereby computationally mimicking the experimental diffusion bonding involved in bi-crystal fabrication. This computationally efficient MD approach employed a classical empirical potential which had been fitted to DFT-computed forces, and properly described the relative energies of a number of metastable alumina polymorphs , ranking the α-Al_2O_3 (corundum) structure as the most stable, unlike most preceding models (23).

For both boundaries, several thousand such MD runs revealed hundreds of metastable boundary structures with reasonably low boundary energies (~1.85 to ~2.35 J/m^2), of which the twenty one with the lowest boundary energies were re-calculated explicitly within DFT using the PBE exchange correlation functional (24). The DFT results demonstrated the efficacy of the simulated annealing approach -- the MD simulations using the empirical potential correctly ranked the candidate structures, and indicated, subsequently confirmed by the DFT calculations, that the lowest energy *Σ7m* boundary had a lower energy than the lowest energy *Σ7a* boundary, 1.84 J/m^2 compared to 2.11 J/m^2.

It is significant that the energy of the *Σ7a* boundary, 2.11 J/m^2, is lower than the value found in an earlier calculation (25) of this boundary, 3.99 J/m^2, and is in better agreement with the experimental value of 0.97 J/m^2, which is based on grain-boundary grooving measurements. This is attributed to the simulated annealing protocol, which allowed many more local atomic structures of the boundary to be explored to find the lowest energy structure.

Figures 3 and 4 show the atomic structures of the two low energy *Σ7* boundaries. Consider first the lower energy Σ*7m* boundary; the core of the boundary can be described as involving alternate stacking of tetrahedral and pyramidal polyhedra. This is seen most clearly in the top left panel of Fig. 3, where a nearly perfect alignment of all atoms is maintained along [0001]. Viewing along [2 -3 1 0] (the top right panel), the two types of columns strictly follow an alternating pattern. Within each column, the tetrahedra and pyramids are separated from each other by an empty octahedral site. This interface structure provides minimal perturbation of the perfect lattice structure of Al_2O_3.

The lowest energy structure of the *Σ7a* boundary (Fig. 4) also contains a significant number of these four- and five-fold coordinated Al ions. While the oxygen atoms are arranged without any apparent regularity, the Al ions form columns along [0001]. Theses columns can be grouped into hexagons and trapezoids, as indicated by the greyed regions in the lower left panel. The *Σ7a* boundary is less ordered than the *Σ7m* boundary, and represents a much greater perturbation of the perfect structure of the adjacent grains than the *Σ7m* boundary; it contains only a subtle regularity.

The densities of states (DOS) of these two boundaries are shown in Figs. 5 and 6. The DOS for the *Σ7m* boundary shows a sharply peaked maximum about 0.25 eV above the top of the valence band; these states are almost entirely due to oxygen ions in pyramidal five-fold coordination in the core of the boundary. There are also a number of unoccupied states below the single crystal conduction band minimum, causing significant narrowing of the band gap.

The details of the DOS for the *Σ7a* boundary (Fig. 6) are different. There are many more grain boundary states extending ~ 0.6 eV into the gap from the top of the valence band, and these arise from oxygen in tetrahedral coordination, oxygen in pyramidal coordination, and "one-way" coordinated (OWC) oxygens associated with 5-fold coordinated Al (12). The density of empty states near the top of the gap, arising from Al ions in the grain boundary core, is again substantial. The changes in the DOS between the two Σ7 boundaries suggest that random high-angle grain boundaries will have even more near-band edge grain boundary states.

We next consider the effect of Y_2O_3 segregation on the DOS of a *Σ7m* boundary. Because the structure of the boundary shown in Fig. 3 is highly ordered, a dramatic change in atomic and electronic structure is not expected if an Al^{3+} ion is replaced by a Y^{3+} ion. Further, if such a boundary arose stochastically during the course of sintering Al_2O_3, the crystal-like regularity in the structure shown in Fig. 3 would probably render Y_2O_3 segregation unlikely.

We thus chose to study the effect of Y_2O_3 segregation using an alternative *Σ7m* boundary structure generated using a standard geometry optimization, rather than the full "Stimulated Annealing" MD calculation. This simplified procedure allows for only relatively small changes in the atomic positions, and effectively immobilized some ions at unfavourable positions in the grain boundary core region. The energy of this metastable *Σ7m* boundary structure, 2.28 J/m^2, can be compared to the energy of the *Σ7m* boundary shown in Fig. 3, 1.84 J/m^2.

The structure of this boundary is shown in Fig. 7a; it is comparable to the lowest energy "annealed" structure shown in Fig 3 with respect to the apparent columnar alignment of the Al in the grain boundary core region; however, the arrangement of the four- and five-fold coordinated Al ions differs significantly from that of the lowest energy structure. Thus, it seems to be a reasonable choice for exploring the structural and electronic effects of Y segregation.

In a series of further simulations, one Al^{3+} ion in the structure of this un-doped boundary was replaced with a Y^{3+} ion and the ionic forces minimized. This was done for a number of different Al ions in the grain boundary core, and the atomic structure shown in Fig. 7b had the lowest energy. The important structural information shown in this figure is that Y in the grain boundary core has the same coordination as Y in $Y_3Al_5O_{12}$ (YAG), with Y-O distances varying from 0.22 to 0.28 nm.

The DOS for the un-doped and Y-doped *Σ7m* boundaries are shown in Fig. 8. Yttrium in the boundary, although iso-electronic with aluminum, allows the structure to relax in such a way as to virtually eliminate the energetically unfavorable five-fold coordination of some of the Al ions. This attenuates the density of oxygen grain boundary near-band edge defect states extending into the gap from the top of the valence band. Again, there are also a number of unoccupied states below the

conduction band minimum, which arise predominantly from the Al ions in the grain boundary core region.

Although the geometry optimization for the Y-doped boundary lacks the rigor of the Simulated Annealing procedure, these calculations demonstrate how the Y dopants can eliminate unfavorable local atomic configurations by forming additional chemical bonds unavailable to the Al ions, and illustrate how the atomic and the electronic structures are inextricably intertwined.

While these important consequences of Y-doping have been demonstrated for this highly structured Y-doped boundary, similar changes in the band structure can be anticipated for any grain boundary in Al_2O_3 containing segregated Y_2O_3. In fact, it is this feature of the DOS that we suggest bears on the reduction on δD_b^{oxy} by $\sim 1/3$ in the permeability experiments, due to Y^{3+} doping (19.) The dearth of available states close to the Fermi level most likely restricts the counter-flow of the electronic defects (electrons or holes) required to keep the two surfaces of the permeability specimens in a quasi-steady-state of excess charge, as charged oxygen or Al vacancies are transported from one surface to the other.

IV. High Temperature Creep Resistance of Polycrystalline Al_2O_3

The improvement in high temperature creep resistance by doping polycrystalline Al_2O_3 with Y_2O_3, ZrO_2, and rare earth sesquioxides (Fig. 9) was a particularly active area of research in the 1990's (see refs. 1 and 2). As noted in the Introduction, the consensus in the field in the intervening years is that these oversize ions segregate to grain boundaries and block critical diffusion paths.

Table 1 lists the relevant ionic radii for these dopant ions. Comparison of these data with the creep results shown in Fig. 9 reveals a poor correlation between the improved creep resistance and ionic radii; for example, Y^{3+} is more efficacious than Nd^{3+}, although Nd^{3+} is the larger specie. Clearly, steric considerations cannot be the whole story. However, all dopants did improve the creep resistance of polycrystalline Al_2O_3.

We suggest that a dearth of near-band edge defect states arising from grain boundary segregation of Y_2O_3 (and other dopant oxides), as shown so strikingly in Fig. 8, affects production/annihilation of the ionic point defects (vacancies and/or interstitials) that are an essential component of the deformation mechanism(s) involved in the high temperature creep. A second important factor involves the grain boundary disconnections, which are thought to mediate grain boundary diffusion in Al_2O_3 (see below). Given that the creep resistance can improve by nearly three orders of magnitude, these oversized solutes must hinder migration of grain boundary disconnections in a straightforward solution hardening sense.

It is also probable that the apparent $(\text{stress})^2$ behavior that is a striking aspect of the high-temperature creep of fine-grained Al_2O_3 ceramics (Fig. 9) is an inherent feature of disconnection-mediated creep. Disconnection motion at grain boundaries certainly

provides a shear deformation mechanism analogous to dislocation motion within a grain. Furthermore, the self-energy of a disconnection is typically much smaller than that for a lattice dislocation, due to the generally smaller Burgers' vectors (11), so disconnections should be relatively easy to form and propagate under the modest stresses typically used for Al_2O_3 during high temperature creep experiments.

Conventional power law dislocation creep is rarely if ever observed for Al_2O_3, (26, 27), nor is conventional Coble (Newtonian) creep (28); rather a $(stress)^2/(grain\ size)^3$ dependence is most frequently observed (this behavior is often described as diffusion-driven superplasticity).

The origin of the stress dependence during high temperature creep deformation is an unsolved problem in metals (29), and the situation is not much better for ceramics. The conventional phenomenological power law creep models that are used to explain $(stress)^3$ or $(stress)^{4.5}$ creep behavior are not relevant for fine-grained Al_2O_3 under modest stresses. The most recent attempt (30) to explain these grain size and stress dependencies involves a model that assumes that grain curvature is the driving force for grain sliding, that grain boundaries are dislocation-free, and that grain boundary sliding is accommodated by diffusion. As has been argued earlier, at least for Al_2O_3, these assumptions may be in doubt, as we believe that such high temperature deformation in polycrystalline Al_2O_3 must involve, at least in part, shear-driven disconnection migration.

It is very likely that a disconnection shear/grain boundary climb accommodation model that resemble existing creep models, but that give a $(stress)^2/(grain\ size)^3$ dependence, could be formulated for Al_2O_3 and other high temperature ceramics, but that must remain a topic for future research.

V. **The Reactive Element (RE) Effect in Al_2O_3-Scale Formation in Ni-base and Fe-base Alloys**

Band structure notions may also be involved in the RE effect in Al_2O_3 scale-forming alloys (10, 11). (As already noted, these REs segregate to grain boundaries in Al_2O_3 scales and are from the same family of oxides that improve the high temperature creep resistance of Al_2O_3.) Although the RE effect has been known for over half a century, explanations have been for the most part "hand waving", some of which have involved similar (unpersuasive) steric explanations (e.g. "site blocking") for the improved oxidation resistance.

Figure 10 shows a particularly insightful data set (7). Steric considerations cannot explain why 0.05 at. % Y in the γ/γ′ alloy affords better oxidation resistance than 0.1 at. % and why Hf is a "better" RE than Y. Figure 2 shows that HfO_2 doping of Al_2O_3 had no effect on permeability-derived oxygen grain boundary diffusivity, but did decrease Al grain boundary diffusivity by a factor of ~2. Although the presence of monoclinic

HfO_2 grain boundary precipitates complicates the story, the permeability data can be taken as good evidence that δD_b^{Al} is reduced by Hf segregation.

While there is no doubt that the oxidation data in Fig. 10 must have involved scale growth by enhanced grain boundary diffusion, it is not clear why Hf is such an effective RE compared to Y. Conventional wisdom in the ceramic science and high temperature oxidation communities takes it that dissolution of HfO_2, either in the lattice or at grain boundaries, would generate Al vacancies (Eqn. [4]), and thus enhance both lattice and, by extension, grain boundary diffusion of Al.

$$3HfO_2 \rightarrow 3Hf_{Al}^{\bullet} + 6O_o^x + V_{Al}''' \qquad [4]$$

This view is clearly at variance with the data of Figs. 1, 2 and 10. Furthermore, so-called double oxidation experiments (31) have revealed that oxidation of alloys lacking REs involve new scale formation at both the scale/gas and scale/substrate interfaces, while in RE-containing alloys, outward Al diffusion (inward diffusion of Al vacancies), is almost completely suppressed (3, 31). Clearly, Eqn. [4] cannot be correct, at least for Hf segregation to Al_2O_3 grain boundaries.

This puzzle could be resolved if the charge compensation necessary in the case of HfO_2 segregation to Al_2O_3 grain boundaries was described by Eqn. [5a] and Eqn. [5b] and not Eqn. [4].

$$HfO_2 + h^{\bullet} \rightarrow Hf_{Al}^{\bullet} + 2O_O^x \qquad [5a]$$

$$2HfO_2 + 2h^{\bullet} \rightarrow 2Hf_{Al}^{\bullet} + 3O_O^{\times} + \tfrac{1}{2}O_2(g) \qquad [5b]$$

Egns. [5a] and [5b] refer specially to grain boundary regions; the former does not preserve site balance in the sense emphasized using Kröger-Vink (KV) notation for the defect chemistry of Al_2O_3, whereas the latter maintains cite balance at the expense of releasing O_2 gas to the environment.

Whether KV reaction always stand for real chemical reactions, or instead represent two options for balancing charge in a system, is a subtle question. In other word since a random high angle grain boundary has, almost by definition, no proscribed crystal structures, does this offer an extra degree of freedom regarding site balance.

In a simple mixture of HfO_2 and Al_2O_3 at a grain boundary, Eqn. [5a] says that the Hf could either adopt its 'natural' 4+ charge state, as in the right hand side, or it can release a hole and adopt the same charge state as Al, namely 3+, as on the left hand side of the equation. Oxygen may or may not leave the system to the vapour phase (Equ. [5b]).

The issue seems to be the energy for Hf to switch its ionisation states, so the reaction of interest is Equ [5c]. If Hf3+ finds itself in the boundary, where there are generally more

holes around than in bulk alumina, it will absorb them, probably binding in some oxygen in the process. Incorporation of Hf at the boundary doesn't have to release oxygen (Equ. [5b]), but if it is carrying with it an 'excess' of oxygen compared to the M2O3 formula, it could be an indirect trap for holes in the sense that oxygen ions pick up holes and leave with them as oxygen gas. Or is the Hf there without an excess of oxygen, but in the 3+ state, i.e. in a sense substituting for Al, but from that state it readily traps holes directly and converts to 4+ whatever the case, either picture reduces the conductivity of the boundary compared to the undoped case.

$$Hf^{4+} \leftrightarrow Hf^{3+} + h^{+} \qquad [5c]$$

Equations [5a] or [5b] are further arguments, if such are needed, that band structure considerations involving the electrons and holes needed to ionize oxygen at the scale/gas interface and Al at the scale/metal interface are at the heart of the RE effect. However, DFT calculations are needed to confirm the plausibility and implications of these equations.

VI. Enhanced Grain Boundary Diffusion in Al_2O_3

Figure 11 is a compilation of all reliable* tracer diffusion data for lattice and grain boundary diffusion in Al_2O_3 known to the authors (32)**. For the grain boundary diffusion experiments, fully dense, high purity polycrystalline Al_2O_3 with two different grain sizes were used -- D_b^{Al} was studied in a material with ~1μm average grain size, while study of D_b^{oxy} utilized samples with ~10μm grain size. These data are described more fully elsewhere (32).

Although the data are sparse, the enhancement in the ^{26}Al tracer-derived D_b^{Al} data, relative to the lattice diffusion data, D_l^{Al}, is nearly a factor of 10^5. The oxygen diffusion data is much more extensive, reflecting the ready availability of ^{18}O as a convenient tracer, compared to the rather scarce ^{26}Al tracer, and show even greater enhancement compared to the lattice diffusion data, D_l^{oxy}, up to a factor of ~10^8! Quite different from the lattice diffusion data, D_b^{Al} and D_b^{oxy} have comparable magnitudes over a wide temperature range. Furthermore, and as noted in ref. (33), the pre-exponentials for both D_b^{Al} and D_b^{oxy} are orders of magnitude too large to be consistent with a point defect mechanism, an important finding which we return to below. Lastly, the activation energies appear to be equal to or greater than those for lattice diffusion.

**The study of D_b^{oxy} in un-doped and Y_2O_3 –doped polycrystalline Al_2O_3 cited earlier (5) is not considered further in this paper. The pre-exponential and activation energy for the un-doped material are both so large as to appear unphysical. This is perhaps related to the lack of full density in the un-doped material (96% of theoretical) and the heterogeneous grain size in both materials (see Fig. 2 in ref. (5)).*

***A full discussion of the lattice diffusion data, D_l^{Al} and D_l^{oxy}, is included in ref. (32).*

The wide scatter in polycrystalline D_b^{oxy} data, nearly a factor of 10^2 at any temperature is not due to experimental scatter but to real differences in D_b^{oxy} in adjacent random, high-angle grain boundaries surrounding a given grain (see Fig. 9b in ref. (11)) . It has been possible (32) to acquire data from 5 randomly chosen close-by grain boundaries at two different temperatures and Arrhenius equations have been fit to the data (Fig. 11); among these 5 boundaries, the activation energies ranged from 405 to 695 kJ/mol and the pre-exponentials from 1.3 to 1.5×10^8. All grain boundaries are clearly not equal when it comes to enhanced diffusion. (For these experiments, samples were sintered to full density at 1800˚C; the first diffusion experiment was performed at 1500˚C. After determining the ^{18}O depth profile, the region containing ^{18}O was carefully polished away, and a second $^{18}O_2$ diffusion experiment was performed at 1650˚C. Microstructural examination showed that a group of reasonably straight boundaries had not appreciably migrated during the second diffusion run and provided the D_b^{oxy} data connected by straight lines in the inset in Fig. 11.

Turning now to the bi-crystal data (6, 13), several aspects are worthy of note. Firstly, while oxygen diffusion is enhanced in these highly structured grain boundaries, they only show a factor of $\sim 10^4$ enhancement relative to oxygen lattice diffusion, compared to the $\sim 10^8$ increase for random grain boundaries in polycrystalline Al_2O_3. While such bi-crystal boundaries are interesting in their own right, they are not particularly good model materials for understanding diffusion in high angle grain boundaries in Al_2O_3. The sluggish diffusion kinetics relative to polycrystalline oxygen grain boundary diffusion must reflect important differences in the basic grain boundary diffusion mechanism(s).

Secondly, data exists for two different, ostensibly identical, un-doped *Σ31* boundaries. Although both were fabricated from high purity (>99.9 wt %) Verneuil crystals supplied by the same vendor (Shinkosha Co. Ltd., Japan), different parent crystals were used to fabricate the two bi-crystal specimens. This lack of reproducibility is not understood, as the differences in the absolute magnitudes of D_b^{oxy} are much greater than experimental uncertainties.

The Y-doped *Σ31* bi-crystal specimen was fabricated from the crystal showing the larger values of D_b^{oxy}, and caused a reduction in diffusivity of ~10x. Band structure considerations (Section III) are presumably again involved to explain this reduction in D_b^{oxy}.

Thirdly, as in the polycrystalline D_b^{oxy} data, boundary-to-boundary variability is a dominant feature of the bi-crystal data. The *Σ7m* and *Σ7a* symmetric tilt bi-crystal boundaries, which differ only in the orientation of the boundary plane, show, respectively, the highest and lowest activation energies of the bi-crystal specimens, 820 and 540 kJ/mol (13), and differ in their pre-exponentials by $\sim 10^3$. These differences must reflect the significant differences in the atomic structures of the respective boundaries shown in Figs. 3 and 4. The two *Σ21* bi-crystals show a similar but less dramatic effect of the orientation of the boundary plane.

Indirect D_b data derived from oxygen permeability experiments (34) and from high temperature creep experiments (26, 27), are also available and are shown in Fig. 12. We discuss the permeability-derived data first.

Although such experiments provide useful "global" data, given the boundary-boundary variability in the D_b^{oxy} data already discussed, the permeability data always suggest more sluggish kinetics than do the tracer diffusion data. For example, the D_b^{Al} data from the permeability experiments are for an oxygen pressure of 10^5 Pa, and should be directly comparable with the ^{26}Al tracer data. However, the difference in the activation energies, 604 kJ/mol versus 400 kJ/mol, is troubling. Furthermore, extrapolating the permeability data to the temperatures where the tracer data were obtained results in a difference of $\sim 10^2$! We believe that this discrepancy is related to the electric fields that must exist during these permeability experiments.

The permeability-derived D_b^{oxy} data are similarly problematical. After accounting for the $p(O_2)$ dependence, the data suggest up to 2 orders of magnitude more sluggish kinetics than those for Al grain boundary diffusion, and are lower at any temperature, by at least a factor of 10, than the grain boundaries with the lowest tracer diffusivities (see the insets to Figs. 11 and 12).

In fact, and not withstanding the boundary-boundary variability, ^{18}O tracer data obtained in a $p(O_2)$ gradient (10^4 Pa-10^{-8} Pa) were $\sim$10x lower than data obtained from experiments conducted in the same apparatus at a constant $p(O_2)$ of 10^4 Pa (35). This most likely is related to the fact that the charged species providing the mass transport are diffusing against an electric field.

The further reduction in permeability-derived D_b^{oxy} on Y-doping has already been discussed in Section II.

Comparison of the tracer data with D_b data derived from high temperature creep experiments of fine-grained polycrystalline Al_2O_3 (26, 27), are less troublesome. In the original work (27), it was thought that D_b^{oxy} was greater than D_b^{Al}, and that the grain boundary diffusion data derived from the creep experiments was thus for Al. However, Fig. 11 shows that the absolute magnitudes of the tracer data for D_b^{Al} and D_b^{oxy} are comparable. (Comparable magnitudes of D_b^{Al} and D_b^{oxy} are also inferred from the kinetics of Al_2O_3 scale formation in alloys lacking Reactive Elements (10, 11, 31).) Given the complex and simultaneous contribution of interface-controlled diffusional creep, basal slip, and non-accommodated grain boundary sliding to the high temperature creep deformation, it may not be possible to attribute the creep-derived D_b data to a single rate-controlling specie.

As a matter of interest, Fig. 12 also contains data on pipe diffusion in sapphire (short circuit diffusion along dislocation cores), determined indirectly by study of dislocation dipole annihilation (36) and by ^{18}O tracer diffusion measurements (37). There is enhancement by a factor of $\sim 10^5$ compared to lattice diffusion of oxygen, and

remarkably good agreement between the two data sets. It is interesting that the enhancement is significantly less than that exhibited by random high angle grain boundaries.

Finally, and as already mentioned, while vacancies or interstitials are normally assumed to be involved in the mechanism of grain boundary diffusion, the pre-exponential D_{bo} values, assuming δ has the conventional value of 1 nm, are orders of magnitude too high to be consistent with a point defect mechanism (33). We thus conclude that grain boundary diffusion must involve a collective mechanism, rather than a simple point defect hopping mechanism. An interesting candidate mechanism involves migration of a class of grain boundary ledge defects called disconnections (21), which are characterized by a step height h and a Burgers vector $\boldsymbol{b}$. Similar to lattice dislocations**,** the Burgers vector $\boldsymbol{b}$ characterizes the strain field of the grain boundary ledge defect and defines the displacement associated with its motion. In the context of the present discussion, the various grain boundaries will have disconnections with different values of h and $\boldsymbol{b}$, and therefore different mobilities, thus accounting for the unexpected spread in D_b^{oxy} values at any temperature. Further, the Burgers vectors of the disconnections in the highly structured bi-crystal boundaries must be much larger than those in random high-angle boundaries, thus providing a possible and plausible explanation for the sluggish oxygen grain boundary diffusion data relative to D_b^{oxy} values for polycrystalline Al_2O_3.

There is little doubt that disconnections are present in polycrystalline Al_2O_3. Because the Burgers vectors of disconnections are likely to be quite small (11), it is much easier to recognize disconnections by their ledges in the TEM, and Figs. 13 and 14 show disconnections in undoped polycrystalline Al_2O_3 and HfO_2-doped polycrystalline Al_2O_3, respectively (33, 38).

VII. Summary and Conclusions

Y_2O_3 segregation to high angle grain boundaries in polycrystalline Al_2O_3 improves both the high temperature creep resistance of Y_2O_3-doped Al_2O_3, and the oxidation resistance of Y-containing Al_2O_3-scale forming Ni-base and Fe-base alloys (the reactive element (RE) effect), and decreases the oxygen permeation rate. Creation or annihilation of charged vacancies at surfaces, triple-junctions or high angle grain boundaries, which occur during both creep and oxidation, requires the participation of electrons or holes, which arise from near-band edge defect states. Hence, we have suggested that changes in the band structure due to such segregation must be an important factor in the improved performance.

Quantum mechanical DFT calculations of the density of states (DOS) of a $\Sigma 7$ bi-crystal boundary, with and without Y segregation, show that there is a drastic reduction in the concentration of near-band edge states in the Y-doped bi-crystal. This is good evidence that band structure effects must be considered when attempting to explain the efficacy of the Y_2O_3 dopant.

Grain boundary diffusion in Al_2O_3 has also been reviewed. Surprisingly, the activation energies for grain boundary diffusion, D_b, are equal to or greater than that for lattice diffusion. Further, the pre-exponentials are so that large that they preclude the traditional mechanism of grain boundary diffusion based on localized point -defect hopping in the plane of the boundary.

We have suggested that enhanced grain boundary diffusion in Al_2O_3 (and most likely other refractory oxides) occurs by migration of disconnections, a class of grain boundary ledge defects characterized by a step height, h, and a Burgers vector, $\boldsymbol{b}$. Migration of these defects must also be important during high temperature creep of Al_2O_3, and may be involved in explaining the $(\text{stress})^2/(\text{grain size})^3$ dependence of the creep rate, which has been often observed but not adequately explained. With this interpretation, we would regard the 'vacancies' that are produced according to equations (1) and (2) as jogs that migrate along the disconnections, by some as yet unknown cooperative atomic displacements, which might be investigated by atomistic simulation. In any case, we must suppose from the two observed power law dependencies of oxygen permeability on $p(O_2)$, as reported in low and high pressure experiments, that these jogs are carrying the equivalent oxygen or aluminum deficits, together with the charges, of single vacancies. Other mechanisms of ion and associated charge transport are conceivable, such as local fluctuations in the configuration of structural units; events of this kind have been observed, for example, in atomistic simulations of boundaries in Si at elevated temperatures (39). In the case of Al_2O_3, these fluctuating atomic rearrangements might shift the local excess volume and charge they are carrying by increments along the boundary. Further study of such events by computer simulation, to reveal details of the mechanism, might uncover other possibilities for cooperative diffusion that have not yet been imagined.

Acknowlegements

The research at CWRU (AHH and MZA) and at the Univ. of Pittsburgh (BG) was supported by the US Office of Naval Research, Dr. David Shifler, Program Manager. The Imperial College calculations were made with HECToR, the UK's national high-performance computing service, which was provided by UoE HPCx Ltd at the University of Edinburgh, Cray Inc. and NAG Ltd., and funded by the Office of Science and Technology through EPSRC's High End Computing Program; they were enabled by the HPC Materials Chemistry Consortium, which is funded by EPSRC (EP/L000202). Financial support for the Imperial College research (HG, AHH, WMCF, and MWF) was provided by the Leverhulme Foundation (Project F/ 07 058/BSTN), with additional support from the Thomas Young Centre under grant TYC-101.Financial support for TN (Kyoto University) and YI (Univ. of Tokyo) was provided by the Elements Strategy Initiative for Structural Materials (ESISM) through the Ministry of Education, Culture, Sports, Science and Technology 690 (MEXT) of Japan.

References

[1] J. Cho, C.M. Wang, H.M. Chan, J.M. Rickman, and M.P. Harmer, "Role of Segregating Dopants on the Improved Creep Resistance of Aluminum Oxide," *Acta mater*., **47**, 4197-4207 (1999).

[2] H. Yoshida, Y. Ikuhara, and T. Sakuma, "High-temperature creep resistance in rare-earth-doped, fine grained Al_2O_3," *J. Mater. Res.,* **13**, 2597-2601 (1998).

[3] P.Y. Hou, "Impurity Effects on Alumina Scale Growth," *J. Am. Ceram. Soc.,* **86**, 660-668 (2003); B. Pint, "Optimization of Reactive-Element Additions to Improve Oxidation Performance of Alumina-forming Alloys," *ibid,* 686-695 (2003).

[4] A.H. Heuer, "Oxygen and aluminum diffusion in α-Al_2O_3: How much do we really understand?" *J. Eur. Ceram. Soc.,* **28**, 1495-1507 (2008).

[5] D. Prot, M. LeGall, B. Lesage, A.M. Huntz, and C. Monty, "Self-diffusion in α-Al_2O_3. IV. Oxygen grain-boundary self-diffusion in undoped and yttria-doped alumina poly-crystals," *Philos. Mag. A.,* **73**, 935-949 (1996).

[6] T. Nakagawa, I. Sakaguchi, N. Shibata, K. Matsunaga, T. Mizoguchi, T. Yamamoto, H. Haneda, and Y. Ikuhara, "Yttrium doping effect on oxygen grain boundary diffusion in Al_2O_3." *Acta materialia*, **55**, 6627-6633. (2007).

[7] B. Gleeson, to be published in *Oxidation of Metals*.

[8] R.D. Shannon, "Revised effective ionic radii and systematic studies of interatomic distances in halides and chalcogonides," *Acta Crystallographica,* **A 32**, 751. (1976).

[9] J. P. Buban, K. Matsunaga, J. Chen, N. Shibata, W. Y. Ching, T. Yamamoto, and Y. Ikuhara, "Grain Boundary Strengthening in Alumina by Rare Earth Impurities ", *Science,* **311**, 212-215 (2006)

[10] A.H. Heuer, D.B. Hovis, J.L. Smialek, and B. Gleeson,"Alumina Scale Formation: A New Perspective," *J. Am. Ceram. Soc.,* **94,** 146-153 (2011).

[11] A.H. Heuer, T. Nakagawa, M.Z. Azar, D.B. Hovis, J.L. Smialek, B. Gleeson, N.D.M. Hine, H. Guhl, H.S. Lee, P. Tangney, W.M.C. Foulkes, and M.W. Finnis, " On the growth of Al_2O_3 scales," *Acta materialia*, **61**, 6670-6683 (2013).

[12] H. Guhl, H.-S. lee, W. M. C. Foulkes, A. H. Heuer, T. Nakagawa, Y. Ikuhara, and M.W. Finnis, "Strutural and Electrical Properties of Σ7 grain Boundaries in α-Al_2O_3", *Acta materialia,* **99**, 16-28 (2015).

[13] T. Nakagawa, H. Nishimura, I. Sakaguchi, N. Shibata, K. Matsunaga, T. Yamamoto, *et al*. "Grain boundary character dependence of oxygen grain boundary diffusion in α-Al_2O_3 bicrystals," *Scripta materialia,* **65**, 544-547(2011).

[14] T. Matsudaira, M. Wada, S. Kitaoka, T. Asai, Y. Miyachi, and Y. Kagiya, "Gas Permeability of Oxide Ceramics at Ultra-High Temperatures," *J. Soc. Mater. Sci. Jpn*., **57**[6] 532-538 (2008).

[15] S. Kitaoka, T. Matsudaira, and M. Wada, "Mass-Transfer Mechanism of Alumina Ceramics under Oxygen Potential Gradients at High Temperatures," *Mater. Trans*., **50**, 1023-1031 (2009).

[16] M. Wada, T. Matsudaira, and S. Kitaoka, "Mutual Grain-boundary Transport of Aluminum and Oxygen in Polycrystalline Al_2O_3 under Oxygen Potential Gradients" , *J. Ceram. Soc. Japan,* **119,** 832-839 (2011).

[17] T. Matsudaira, M. Wada, T. Saitoh, and S. Kitaoka, "The effect of lutetium dopant on oxygen permeability of alumina polycrystals under oxygen potential gradients at ultra-high temperatures," *Acta materiaia*, **58**, 1544-1553 (2010).
[18] T. Matsudaira, M. Wada, T. Saitoh, and S. Kitaoka, "Oxygen permeability in cation-doped polycrystalline alumina under oxygen potential gradients at high temperatures," *Acta materialia,* **59**, 5440-5450(2011).
[19]T. Matsudaira, M. Wada, and S. Kitaoka, "Effect of Dopants on the Distribution of Aluminum and Oxygen Fluxes in Polycrystalline Alumina Under Oxygen Potential Gradients at High Temperatures," *J. Am. Ceram. Soc.,* **96**, 3243-3251 (2013).
[20] S. Kitaoka, T. Matsudaira, M. Wada, T. Saito, M. Tanaka, and Y. Kagawa, Control of Oxygen permeability in Alumina by Oxygen Potential Gradients at High Temperatures by Dopant Configurations" *J. Am. Ceram. Soc.,* **97**, 2314-2322 (2014).
[21] J. P. Hirth, "Dislocations, Steps, and Disconections at Interfaces", *J. Phys. Chem. Solid*s, **55,** 985-989 (1994).
[22] T. Ogawa, A. Kuwabara, C. A. J. Fishwer, H. Moriwake, K. Matsunaga, and S. Kitaoka, "A Density Functional Study of Vacancy Formation in Grain Boundaries of Undoped α-Al_2O_3 ", *Acta materialia*, **69**, 305-371 (2014).
[23] J. Sarsam, M.W. Finnis, and P. Tangney, "Atomistic force field for alumina fit to density functional theory," *J. Chem. Phys.,* **139**, 204704 (2013).
[24] J. P. Perdew, K. Burke, and M. Ernzerhof, "Generalized Gradient Approximation Made Simple", *Phys. Rev. Letters*, **77**, 3865-3868 (1996).
[25] H. Nishimura, K. Matsunaga, T. Saito, T. Yamamoto, and Y. Ikuhara, "Atomic Structures and Energies of Σ7 Symmetrical Tilt Grain Boundaries in Alumina Bicrystals," *J. Am. Ceram. Soc*., **86**[4] 574-580 (2003).
[26] R.M. Cannon, W.H. Rhodes, and A.H. Heuer, "Plastic Deformation in Fine-grained Alumina (Al_2O_3): I, Interface-controlled Diffusional Creep", *J. Am. Ceram. Soc.,* **63,** 46-53 (1980).
[27] A.H. Heuer, N.J. Tighe, and R.M. Cannon, "Plastic Deformation in Fine-Grained Alumina (Al_2O_3): II, Basal Slip and Non-accommodated Grain-Boundary Sliding", *J. Am. Ceram. Soc.,* **63,** 53-58 (1980).
[28] R.L. Coble,"A Model for Boundary Diffusion Controlled Creep in Polycrystalline Materials," *J. Appl. Phys.,* **34,** 1679 (1963).
[29] F.R.N. Nabarro, "Creep in commercially pure metals," *Acta materialia*, **54**, 263-295 (2006).
[30] D. Gómez-García, E. Zapata-Solvas, A. Domínguez-Rodríguez, and L. P. Kubin, "Diffusion-driven Superplasticity in Ceramics: Modeling and comparison with available data," *Physical Review* B **80**, 214107 (2009)
[31], W.J. Quadakkers, A. Elschner, W Speier, and H. Nickel, "Composition and Growth Mechanisms of Alumina Scales on FeCrAl-based Alloys Determined by SNMS", *Applied Surface Science,* 52 [3-4] 271-287 (1991).
[32] T. Nakagawa, D. Hovis, H. Yoshida, Y. Ikuhara, and A.H. Heuer, to be published.
[33] A. H. Heuer and M. Zahiri Azar, "A Disconnection Mechanism of Enhanced Grain Boundary Diffusion in Al_2O_3", *Scripta materialia*, **102**, 15-18 (2015).
[34] S. Kitaoka, private communication.
[35] T. Nakagawa and S. Kitaoka, to be published.

[36] X. Tang, K. P. D. Lagerlöf and A. H. Heuer, "Determination of Pipe Diffusion Coefficients in Un-doped and Magnesia-Doped Sapphire (α-Al_2O_3): A Study Based on Annihilation of Dislocation Dipoles", *J. Am. Ceram. Soc.,* **86,** 560-564 (2003).
[37] T. Nakagawa, A. Nakamura, I. Sakaguchi, N. Shibata, K.P. D. Lagerlöf, T. Yamamoto, and Y. Ikuhara, *J. Ceram. Soc. Japan,* **114**, 1013-1017 (2006)
[38] Z. Yu, Q. Wu, J.M. Rickman, H.C. Chan, and M.P. Harmer, "Atomic-resolution observation of Hf-doped alumina grain boundaries," *Scripta materialia,* **68**, 703-706 (2013).
[39] S. von Alfthan, K. Kaski, and A. P. Sutton, "Molecular Dynamics Simulations of Temperature-induced Structural Transitions at Twist Grain Boundaries in Silicon", *Phys. Rev.,* **B76,** 245317 (2007).

Fig. 1. ***Oxygen pressure dependence of the oxygen permeability in a $p(O_2)$ gradient at 1650 ˚C in dense polycrystalline Al_2O_3, and in similar samples doped with 0.1% Lu_2O_3 or 0.1% HfO_2. Oxygen gas dissolved in the Al_2O_3 from the high pressure ambient and was released from the Al_2O_3 into the low pressure ambient (18).***

Fig. 2. ***Permeability-derived grain boundary diffusion data (δD_{gb}) at 1650˚C in undoped, Lu- doped, and Hf-doped Al_2O_3 (18). δ is the grain boundary width, assumed to be 1 nm.***

Fig. 3. ***Lowest energy structure of a Σ 7m symmetric tilt bi-crystal boundary in Al_2O_3. The computed and experimental grain boundary energies are 1.84 and 1.29 J/m^2, respectively (12).***

Fig. 4 ***Lowest energy structure of a Σ 7a symmetric tilt bi-crystal boundary in Al_2O_3. The computed and experimental grain boundary energies are 2.11 and 0.97 J/m^2. This boundary is "wider" and less well "ordered" than the Σ 7m boundary (12).***

Fig. 5. ***DFT calculation of the density of the states (DOS) of the Σ7m bi-crystal boundary (12).***

Fig. 6. ***DOS of the Σ 7a bi-crystal boundary (12)*.**

Fig. 7a ***Atomic Structure of a metastable Σ 7m bi-crystal boundary.***

Fig. 7b ***Atomic structure of the metastable Σ 7m bi-crystal boundary containing segregated Y.***

Fig. 8. ***DOS of the metastable Σ7m boundary. (a) shows the un-doped boundary and (b) the boundary containing a Y segregant . Note the strong effect of this dopant on the density of oxygen grain boundary states, which arises from a reduction in the number of 5-fold coordinated polyhedral.***

Fig. 9. ***High temperature creep resistance of polycrystalline Al_2O_3 (1, 2). Note that doping Al_2O_3 with Y_2O_3, ZrO_2 and rare earth oxides such as La_2O_3, Nd_2O_3 and Lu_2O_3 dramatically improves the creep resistance. Note also the $(stress)^2$ behavior.***

Fig. 10. ***Reactive element (RE) effect: isothermal oxidation kinetics at 1150°C (single doped - Hf vs. Y). Data of Gleeson et al., Univ. of Pitt. (7).***

Fig. 11. Lattice and grain boundary diffusion data for Al_2O_3 (32). The parallelogram containing data with the highest values of D_b^{ox} is shown in an expanded version as an inset labeled D_b^{oxy}. The bi-crystal data is from refs. (6) and 13).

Fig. 12. Comparison of Permeability-derived and Creep-derived D_b Data.
Fig. 13. Disconnections (arrowed) in a high angle grain boundary in Al_2O_3. The high resolution TEM image has been Fourier-filtered to clearly show the steps ; the selected area diffraction pattern of the left hand grain shows that it is oriented to a <2-201> zone axis. The right hand grain is 4° from a <41-50> zone axis, on which the stereographic projection is centered (33).

Fig. 14. High angle annular dark field (HA-ADF) scanning transmission electron micrograph (STEM) of disconnections (arrowed) in a high angle grain boundary in HfO_2-doped Al_2O_3 (38).

Table 1: Crystal Ionic Radii for Dopant Ions in Oxides (8)

Ion	Atomic Number	Ionic Radius (pm)
Al^{3+}	13	67.5
Y^{3+}	39	104.0
Zr^{4+}	40	86.0
La^{3+}	57	100.1
Nd^{3+}	60	112.3
Lu^{3+}	71	100.1

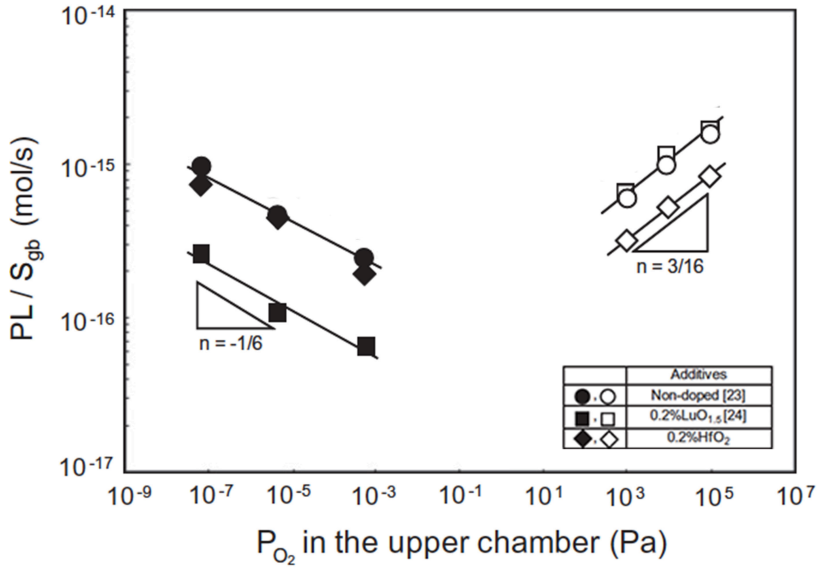

Fig. 1. ***Oxygen pressure dependence of the oxygen permeability in a p(O_2) gradient at 1650 ˚C in dense polycrystalline Al_2O_3, and in similar samples doped with 0.1% Lu_2O_3 or 0.1% HfO_2. Oxygen gas dissolved in the Al_2O_3 from the high pressure ambient and was released from the Al_2O_3 into the low pressure ambient (18).***

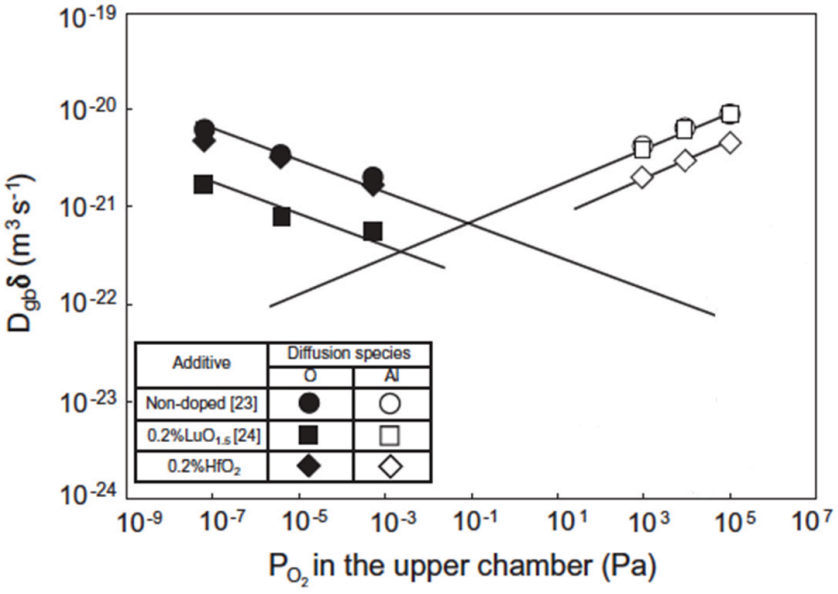

Fig. 2. ***Permeability-derived grain boundary diffusion data (δD_{gb}) at 1650˚C in undoped, Lu- doped, and Hf-doped Al_2O_3 (18). δ is the grain boundary width, assumed to be 1 nm.***

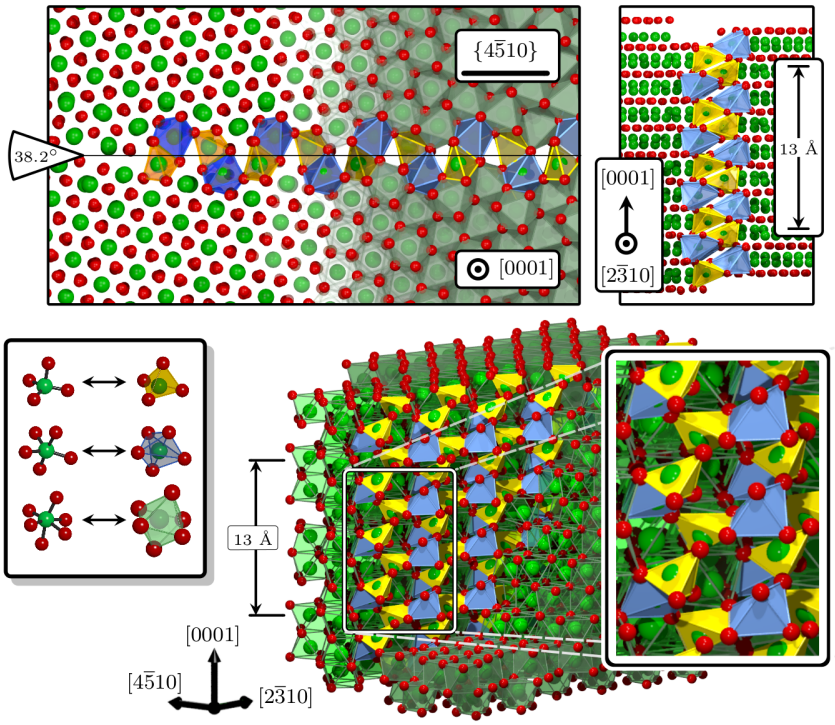

Fig. 3. ***Lowest energy structure of a Σ 7m symmetric tilt bi-crystal boundary in Al_2O_3. The computed and experimental grain boundary energies are 1.84 and 1.29 J/m², respectively (12).***

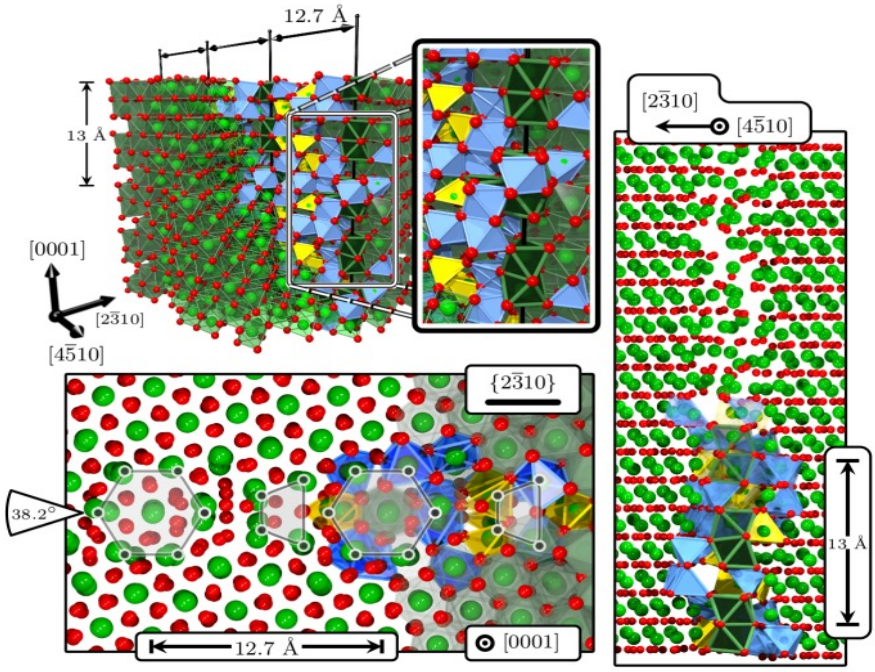

Fig. 4. ***Lowest energy structure of a Σ 7a symmetric tilt bi-crystal boundary in Al_2O_3. The computed and experimental grain boundary energies are 2.11 and 0.97 J/m². This boundary is "wider" and less well "ordered" than the Σ 7m boundary (12).***

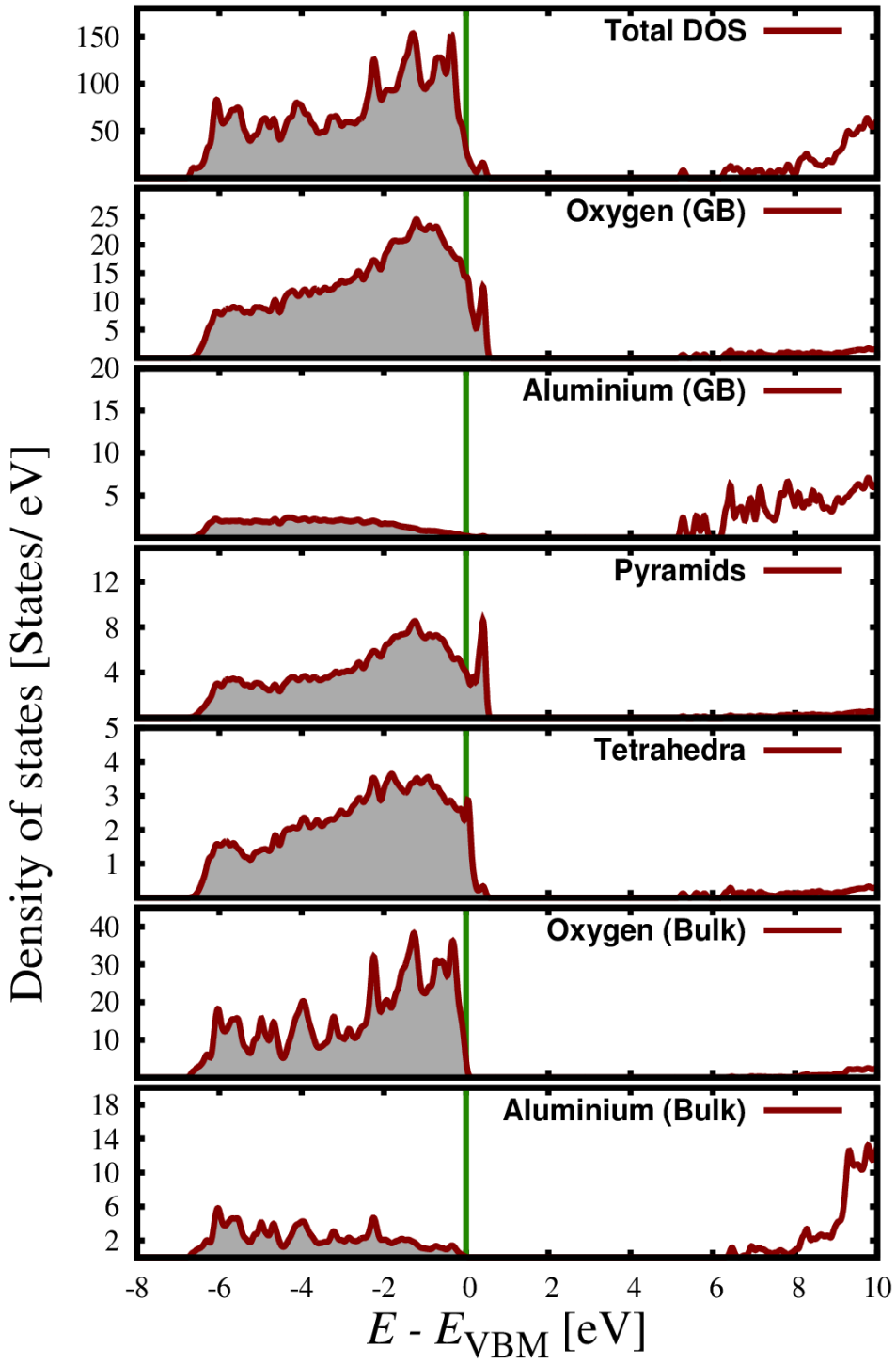

Fig. 5. ***DFT calculation of the density of the states (DOS) of the Σ7m bi-crystal boundary (12).***

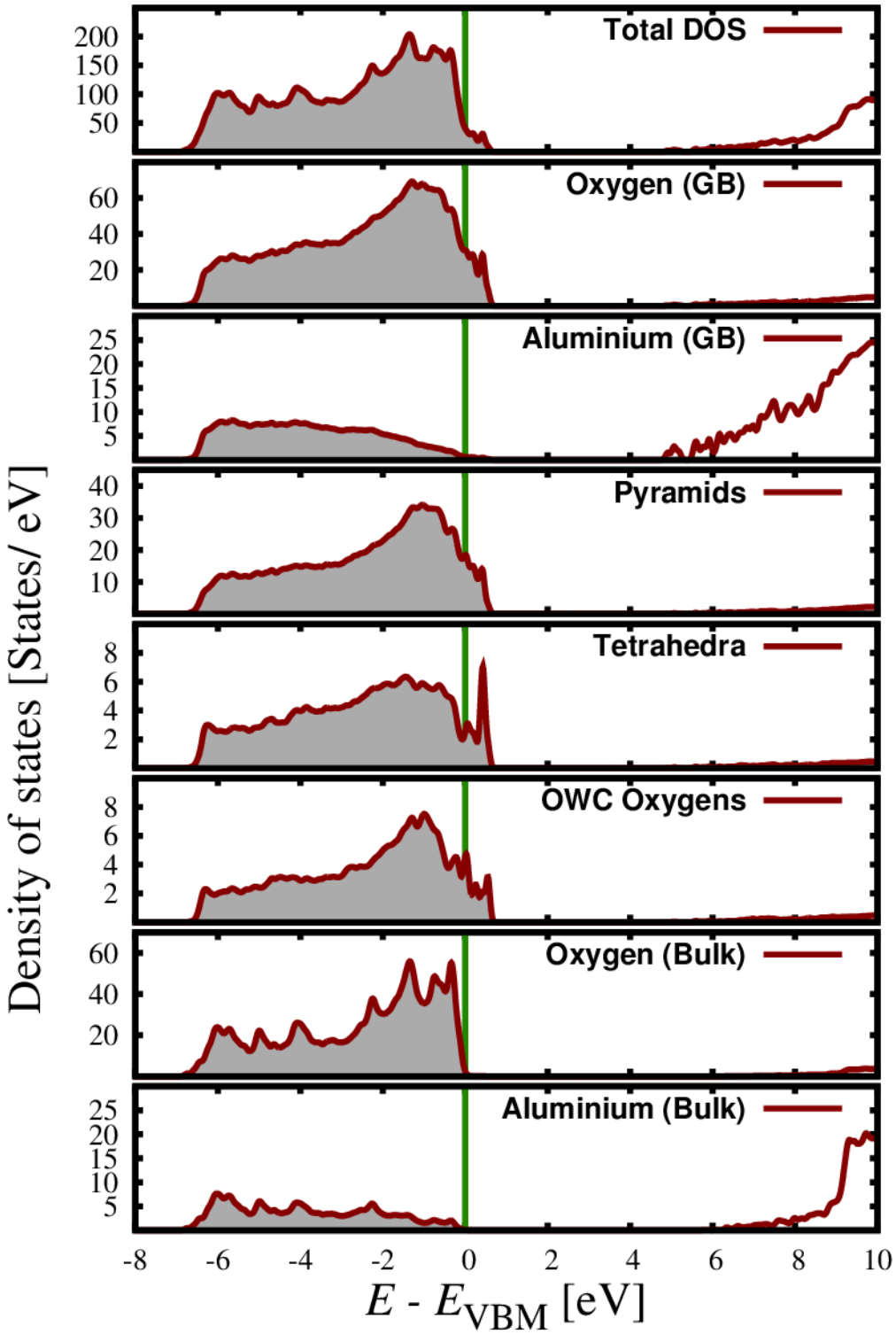

Fig. 6. ***DOS of the Σ 7a bi-crystal boundary (12).***

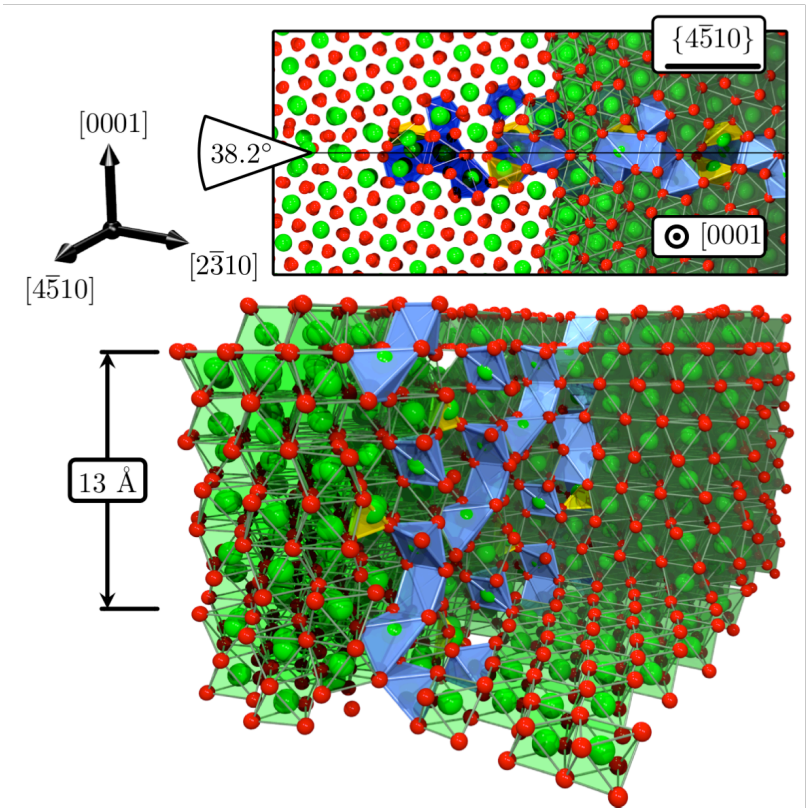

Fig. 7a ***Atomic Structure of a metastable Σ 7m bi-crystal boundary.***

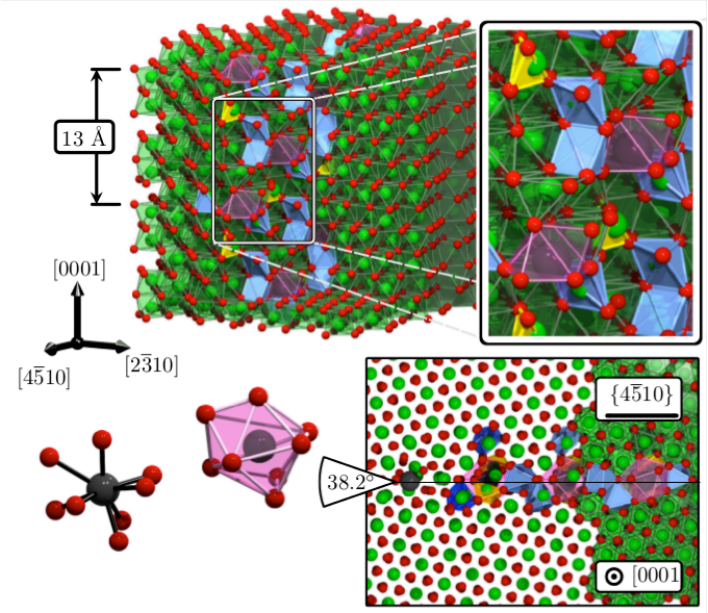

Fig. 7b ***Atomic structure of the metastable Σ 7m bi-crystal boundary containing segregated Y.***

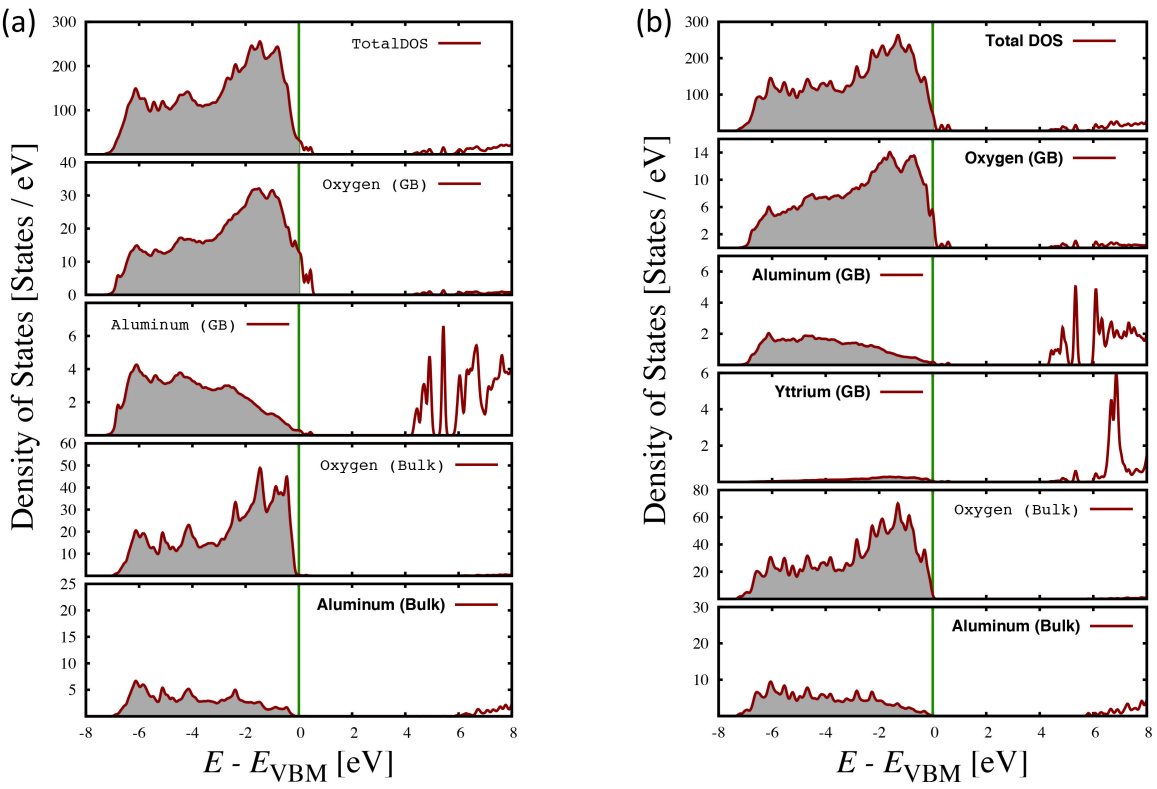

Fig. 8. ***DOS of the metastable Σ7m boundary. (a) shows the un-doped boundary and (b) the boundary containing a Y segregant . Note the strong effect of this dopant on the density of oxygen grain boundary states, which arises from a reduction in the number of 5-fold coordinated polyhedral.***

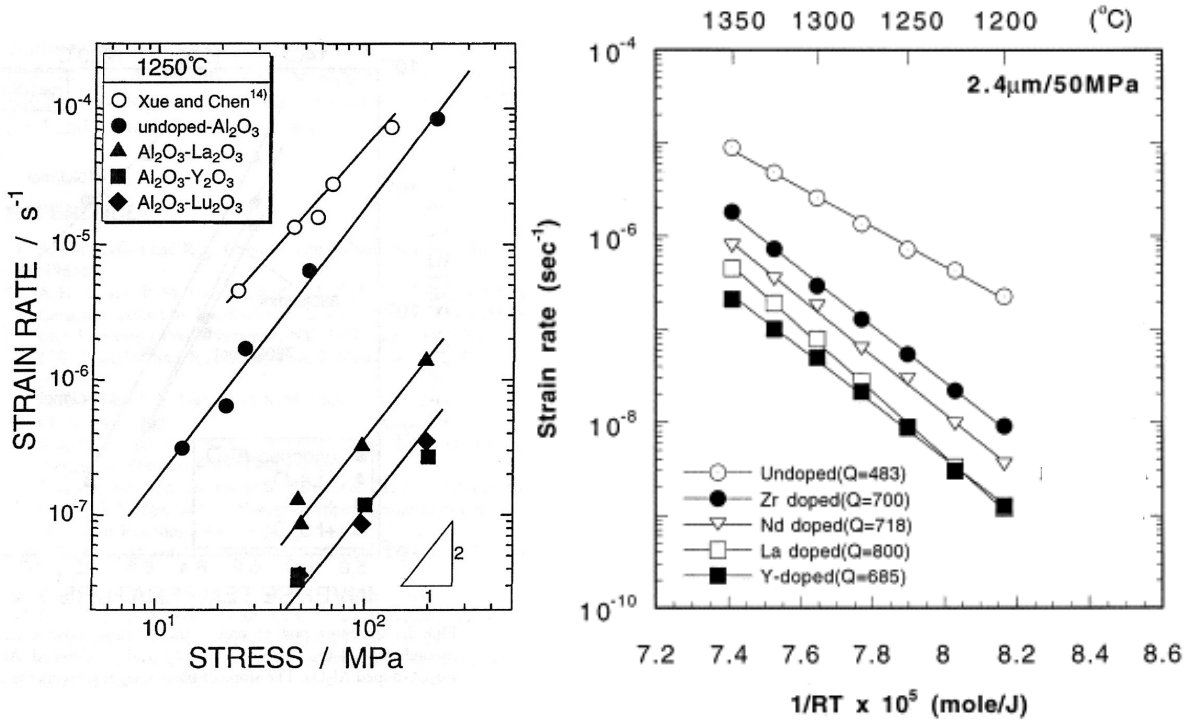

Fig. 9. ***High temperature creep resistance of polycrystalline Al_2O_3 (1, 2). Note that doping Al_2O_3 with Y_2O_3, ZrO_2 and rare earth oxides such as La_2O_3, Nd_2O_3 and Lu_2O_3 dramatically improves the creep resistance. Note also the (stress)^2 behavior.***

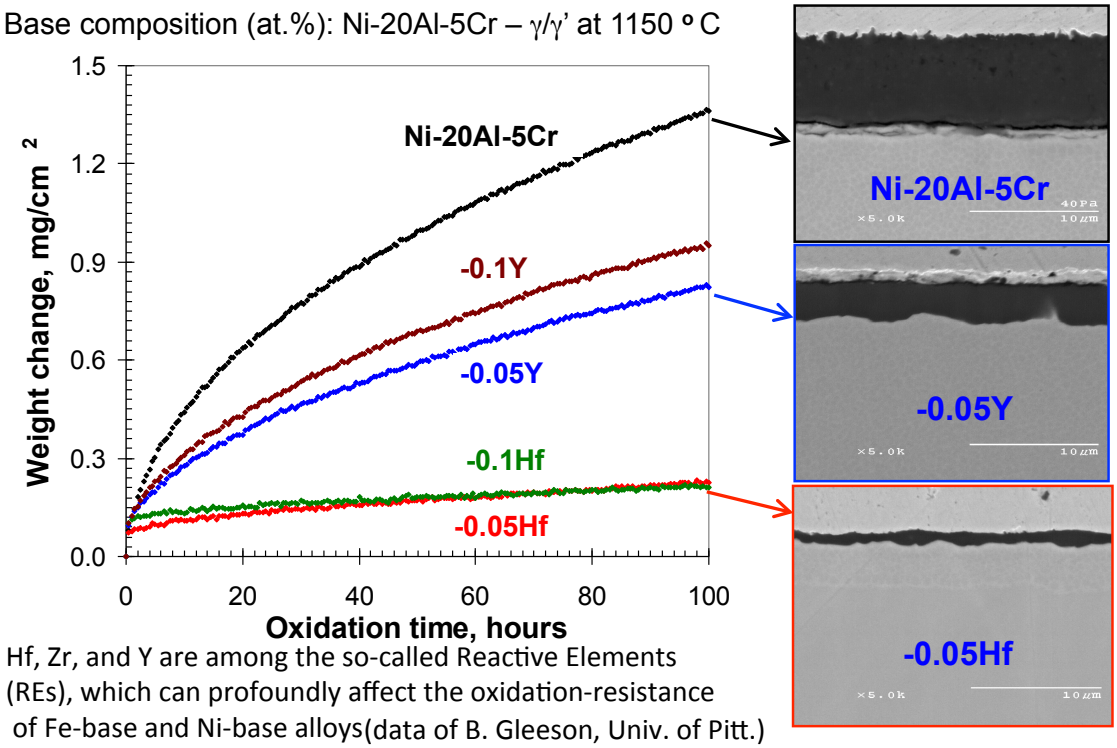

Fig. 10. ***Reactive element (RE) effect: isothermal oxidation kinetics at 1150ºC (single doped - Hf vs. Y). Data of Gleeson et al., Univ. of Pitt. (7).***

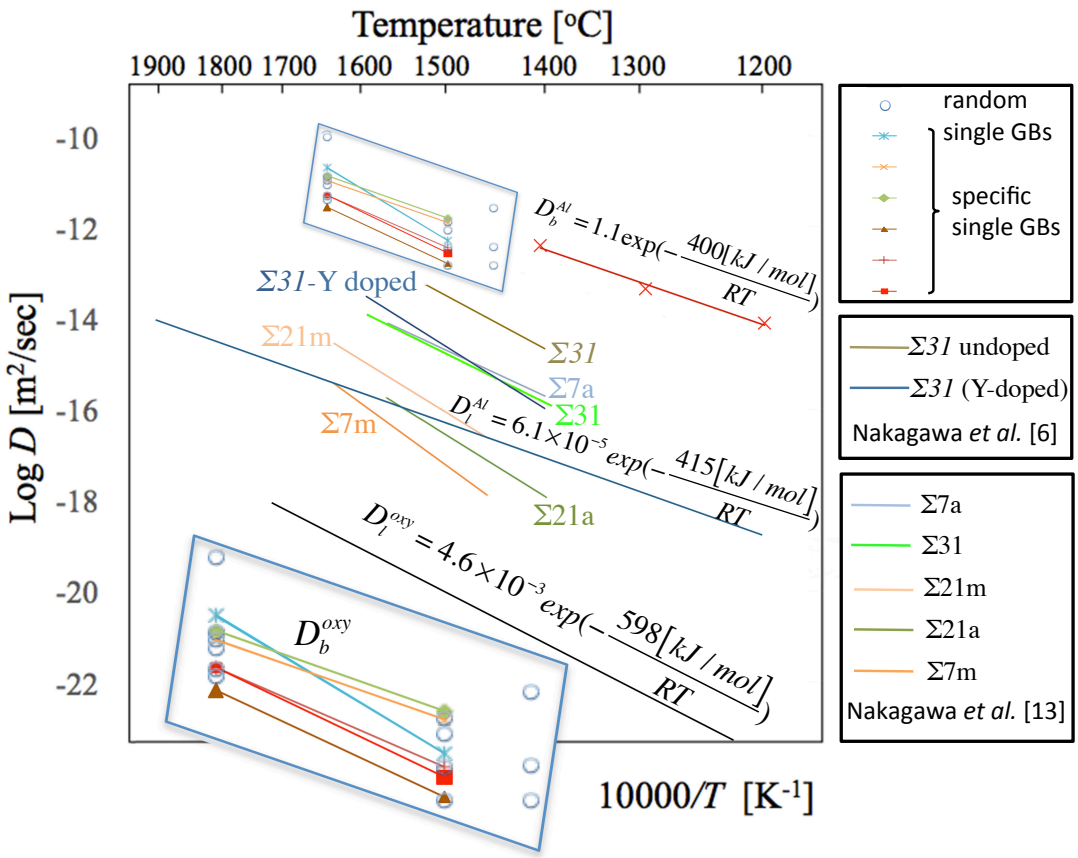

Fig. 11. Lattice and grain boundary diffusion data for Al_2O_3 (32). The parallelogram containing data with the highest values of D_b^{ox} is shown in an expanded version as an inset labeled D_b^{oxy}. The bi-crystal data is from refs. (6) and 13).

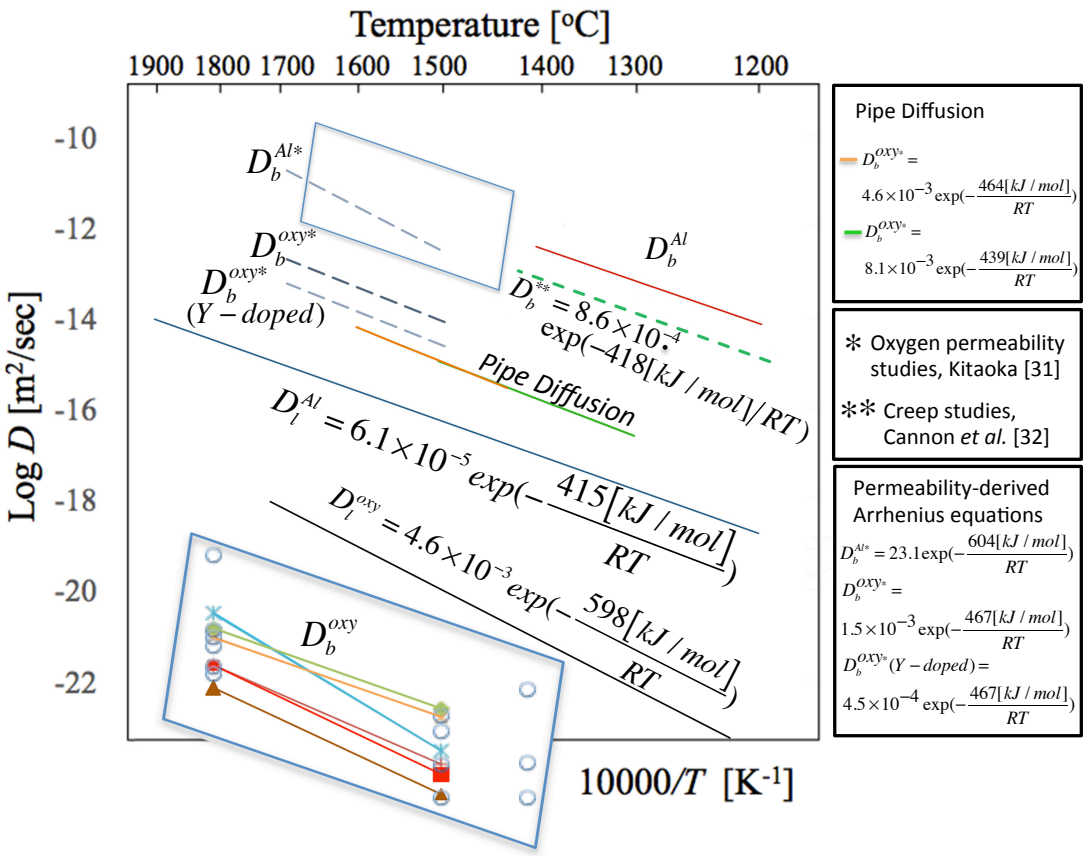

Fig. 12. Comparison of Permeability-derived and Creep-derived D_b Data.

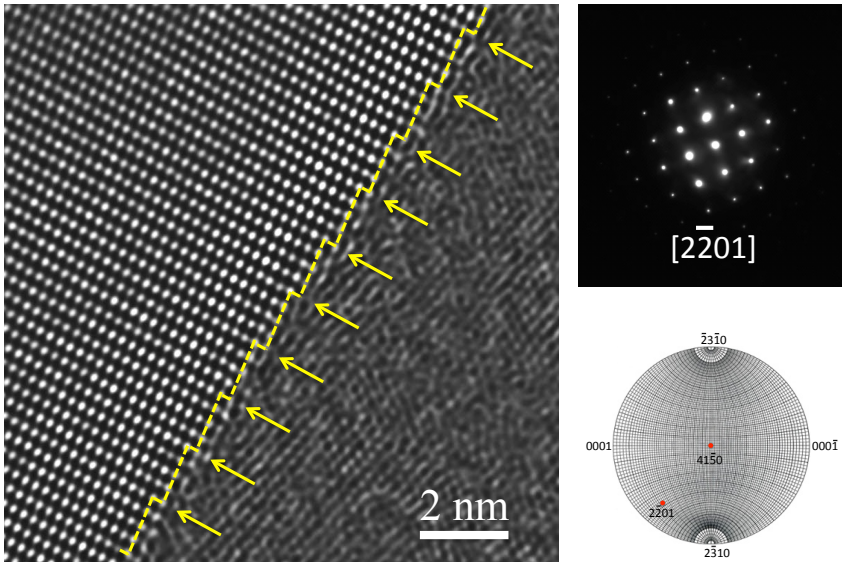

Fig. 13. Disconnections (arrowed) in a high angle grain boundary in Al_2O_3. The high resolution TEM image has been Fourier-filtered to clearly show the steps ; the selected area diffraction pattern of the left hand grain shows that it is oriented to a <2-201> zone axis. The right hand grain is 4° from a <41-50> zone axis, on which the stereographic projection is centered (33).

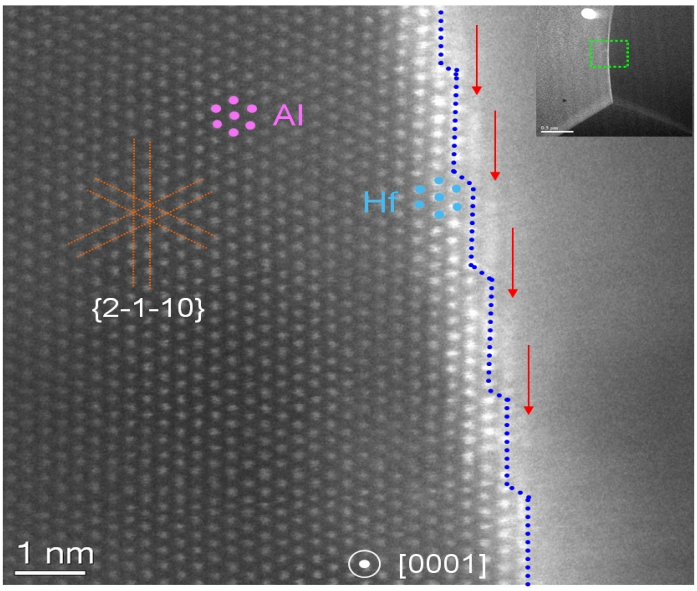

Fig. 14. High angle annular dark field (HA-ADF) scanning transmission electron micrograph (STEM) of disconnections (arrowed) in a high angle grain boundary in HfO_2-doped Al_2O_3 (38).